

Massive Star Formation Starts in Sub-virial Dense Clumps Unless Resisted by Strong Magnetic Fields

KE WANG,¹ YUELLOU WANG,² AND FENGWEI XU^{1, 2, 3}

¹*Kavli Institute for Astronomy and Astrophysics, Peking University, 5 Yiheyuan Road, Haidian District, Beijing 100871, China*

²*Department of Astronomy, School of Physics, Peking University, Beijing, 100871, People's Republic of China*

³*I. Physikalisches Institut, Universität zu Köln Zülpicherstr. 77, 50937 Köln, Germany*

ABSTRACT

The initial conditions are critical for understanding high-mass star formation, but are not well observed. Built on our previous characterization of a Galaxy-wide sample of 463 candidate high-mass starless clumps (HMSCs), here we investigate the dynamical state of a representative subsample of 44 HMSCs (radii 0.13-1.12 pc) using GBT NH₃ (1,1) and (2,2) data from the Radio Ammonia Mid-Plane Survey (RAMPS) pilot data release. By fitting the two NH₃ lines simultaneously, we obtain velocity dispersion, gas kinetic temperature, NH₃ column density and abundance, Mach number, and virial parameter. Thermodynamic analysis reveals that most HMSCs have Mach number < 5, inconsistent to what have been considered in theoretical models. All but one (43/44) of the HMSCs are gravitationally bound with virial parameter $\alpha_{\text{vir}} < 2$. Either these massive clumps are in collapsing or magnetic field strengths of 0.10-2.65 mG (average 0.51 mG) would be needed to support them against collapse. The estimated B-field strength correlates tightly with density, $B_{\text{est}}/\text{mG} = 0.269 (n_{\text{H}_2}/10^4 \text{ cm}^{-3})^{0.61}$, with a similar power-law index as found in observations, but a factor of 4.6 higher in strength. For the first time, the initial dynamical state of high-mass formation regions has been statistically constrained to be sub-virial, in contradictory to theoretical models in virial equilibrium, and in agreement with the lack of observed massive starless cores. The findings urge future observations to quantify the magnetic field support in the prestellar stage of massive clumps, which are rarely explored so far, towards a full understanding of the physical conditions that initiate massive star formation.

Keywords: Star formation (1569), Collapsing clouds (267), Infrared dark clouds (787), Interstellar magnetic fields (845), Interstellar medium (847), Molecular clouds (1072)

1. INTRODUCTION

Corresponding author: Ke Wang
kwang.astro@pku.edu.cn

Massive stars ($M_{\star} \gtrsim 8 M_{\odot}$) play an irreplaceable role in the energy budget and evolution of the Galactic ecosystem. However, their origin remains a fundamental open question. Particularly, the initial conditions are not well constrained by observations, leading to different as-

sumed initial inputs to theoretical models. For example, in the long-standing turbulent core model (McKee & Tan 2002, 2003), massive stars form within massive ($\sim 100 M_{\odot}$) pre-assembled, monolithic (non-fragmenting) cores in highly supersonic turbulence with Mach number $\gtrsim 5$, proceeding in virial equilibrium such that the cores do not collapse free-fall. The model is built on self-similar cores and clumps, where the cores are embedded in clumps, and both share similar dynamical properties (Bertoldi & McKee 1992; McKee & Tan 2002, 2003). In contrast to this “core-fed” scenario, the competitive accretion (Bonnell et al. 2001), global hierarchical collapse (Vázquez-Semadeni et al. 1997), and inertial flow models (Padoan et al. 2020) can be categorized as the “clump-fed” scenario, characterized by gas assembly through either global clump infall and/or coherent and filamentary gas flows (e.g. Peretto et al. 2013; Xu et al. 2023b) that results in massive cluster formation. Both theoretical scenarios require highly turbulent gas; in particular the turbulent core accretion model requires Mach number $M \gtrsim 5$ (McKee & Tan 2003; Krumholz et al. 2007a,b); similar and even higher Mach numbers are adopted in numerical simulations focusing on turbulence regulated star formation, at clump and cloud scales (e.g., Federrath & Klessen 2012). The turbulent core model assume virial equilibrium in self-similar cores and clumps as an initial condition, but do not assume so for protostellar and later evolutionary stages (this has been misinterpreted in some literature). The competitive accretion model requires $\alpha_{\text{vir}} < 1$ for a dynamical, non-equilibrium star formation. It is therefore of critical importance to observe the initial conditions at the pre-stellar stage, before protostars have formed with strong feedback to drastically change the conditions.

Observationally, the early evolution of massive clumps is particularly uncertain, since cold, quiescent clumps are fainter at (sub)millimeter wavelengths and spectral lines than those hosting protostars or even HII regions. For statistically signifi-

cant studies, an unbiased sample of high-mass starless clumps (HMSCs) is necessary. Several studies have made significant efforts to identify reliable HMSCs (e.g., Tackenberg et al. 2012; Traficante et al. 2015; Svoboda et al. 2016; Yuan et al. 2017). Among these, we have presented a sample of 463 HMSCs (Yuan et al. 2017) across the inner Galactic plane ($|l| < 60^{\circ}$, $|b| < 1^{\circ}$), combining ATLASGAL, HiGAL, GLIMPSE, MIPSGAL, and literature data (Benjamin et al. 2003; Carey et al. 2009; Schuller et al. 2009; Csengeri et al. 2014; Molinari et al. 2016a). HMSCs are massive and dense sufficient to form high-mass stars, but have not shown signatures of star formation. Yuan et al. (2017) make source selection through a strict and comprehensive work flow (see their Fig 1). Briefly, we started from all the 10861 ATLASGAL clumps, selecting a flux limited sample (peak flux > 0.5 Jy/beam at $870 \mu\text{m}$) to ensure high-mass, removing clumps with star formation signatures using HiGAL and by querying the SIMBAD database. The signatures include YSOs, IR point sources at $8 \mu\text{m}$, $24 \mu\text{m}$, $70 \mu\text{m}$, extended $70 \mu\text{m}$ emission, (candidate) outflows, masers, “extended green objects”, HII regions, and radio continuum sources recorded in the SIMBAD database (see a full list of 18 signatures in their Table 1). Physical properties of the HMSCs are then derived by pixel-to-pixel SED fitting to combined HiGAL and ATLASGAL data. The 463 clumps satisfying these strict criteria form a complete unbiased sample of HMSCs across the Milky Way disk. Stickily speaking, they should be regarded as candidate HMSCs, because deeply embedded star formation activity may exist (e.g., Feng et al. 2016; Cyganowski et al. 2022; Jiao et al. 2023), and may be under the detection limit of these single-dish shallow surveys. High-resolution interferometric observations are being carried out for this purpose (e.g. Jiao et al. 2023). Nevertheless, these HMSCs represent the earliest observed stages that defines the initial conditions for high-mass star formation.

The 463 HMSCs have a median radii of 0.65 pc and range in 0.05–3.57 pc. For convenience, we refer them as “clumps” throughout this paper, but note that they have a fairly wide range; the smallest of them (20 HMSCs) are actually more appropriate to be called as “cores” (Yuan et al. 2017).

We emphasize that the source selection criteria in Yuan et al. (2017) are the most strict ever employed in studies towards the initial stages. More recent characterization of HiGAL clumps, for example Merello et al. (2019), classify prestellar clumps as those without $70\text{ }\mu\text{m}$ point source. Other potential star formation signatures (e.g., recorded in SIMBAD literature) are not used. Merello et al. (2019) compiled a sample of 1068 HiGAL clumps which have single-pointed NH_3 observations from the literature within half of the corresponding NH_3 beam (mostly from Wienen et al. 2012, see next paragraph). Among those, only 157 are classified as prestellar by the authors, and at most only 19 would satisfy our selection criteria of HMSCs in Yuan et al. (2017). Traficante et al. (2018) compiled a sample of HiGAL 213 clumps with N_2H^+ linewidth from the MALT90 survey, where only 14 clumps are starless.

Wienen et al. (2012) carried out single-pointed NH_3 line observations towards a flux limited (peak APEX $870\text{ }\mu\text{m}$ flux $>0.4\text{ Jy/beam}$) sample of 862 ATLASGAL clumps in the northern sky using the Effelsberg 100 m telescope, with a beam of $40''$ and spectral resolutions of 0.5 and 0.7 km s^{-1} . Although the flux limit is higher than that of Yuan et al. (2017), i.e., the clumps are all considered by our selection, only 43 among the 862 clumps ($<5\%$) fulfill our criteria for HMSCs (as noted in Yuan et al. 2017). Additionally, the sparse spectral resolutions would poorly sample relatively narrow linewidth. Wienen et al. (2018) carried out similar NH_3 observations towards 354 ATLASGAL clumps with peak $870\text{ }\mu\text{m}$ flux $>1.2\text{ Jy/beam}$ in the southern sky using the Parkes 64 m telescope, with a beam of $61''$ and spectral resolutions of 0.4 km s^{-1} . The beamsize is larger than

all the clump sizes, making contamination a potential problem.

Thus, although ~ 1000 unique (massive and low-mass) clumps have been studied by single-pointed NH_3 and N_2H^+ lines, an unusually tiny fraction ($<5\%$) of those are at the starless stage. This is a result of complicated selection bias (Merello et al. 2019). Due to limited observation time, Wienen et al. (2012, 2018) did not complete ATLASGAL sources satisfying their selection criteria; due to sensitivity limit, not all observed sources are detected. The combined selection effect is difficult to characterize. Selection bias in the HiGAL follow-up works are even more difficult to quantify, because the NH_3 observations are not dedicated follow-ups, and thus suffered from different sky coverage, source selection, positional offset, resolution, and completeness, among other issues, as noted in Merello et al. (2019); Traficante et al. (2018). Because of these biases, it is highly questionable whether this tiny fraction of starless clumps is representative of the entire population of starless clumps. Consequently, it is extremely difficult, if possible at all, to identify the initial conditions from these existing results.

The tiny fraction of genuine starless clumps and the associated biases in the aforementioned ATLASGAL and HiGAL follow-up studies reinforces the necessity for a systematic characterization of the dedicated HMSC sample to reveal the initial conditions that would initiate high-mass star formation. Properties of clumps at protostellar and later evolutionary stages presented in these studies provide a highly complementary comparison to investigate how physical conditions may change before and after star formation started.

In this context, we studied the dynamical state of these HMSCs (Huang et al. 2023), using $^{13}\text{CO}(2-1)$ spectra from the SEDIGISM survey (Schuller et al. 2017, 2021; Duarte-Cabral et al. 2021) to obtain linewidth, finding that about half of HMSCs are gravitationally bound. However, CO can be depleted in cold and dense environ-

ments in prestellar stages (Goldsmith 2001; Bergin & Tafalla 2007; Chen et al. 2010; Wang et al. 2012). Also, the optical depth of the ^{13}CO (2–1) line is relatively high. These will lead to a larger linewidth and thus overestimate the kinetic energy. In fact, Huang et al. (2023) already noted that NH_3 linewidth is systematically lower than that of ^{13}CO (2–1). NH_3 is a reliable tracer for cold and dense gas without depletion, for example in infrared dark clouds (IRDCs, Pillai et al. 2006; Zhang & Wang 2011; Wang et al. 2008, 2012, 2014, 2024; Wang & Wang 2023). Figure 1 shows an example HMSC. The NH_3 emission traces the cold and dense clump very well. Moreover, in addition to linewidth, NH_3 lines provide a perfect thermometer, making it excellent to study thermodynamics in HMSCs (Ho & Townes 1983; Walsley & Ungerechts 1983).

In this work, we use NH_3 (1,1) and (2,2) to trace dynamical state and temperature of the $\sim\text{pc}$ scale HMSCs from Yuan et al. (2017), an unbiased, well characterized sample for the initial stages of high-mass star formation.

2. NH_3 DATA AND FITTING

The Radio Ammonia Mid-Plane Survey (RAMPS, Hogge et al. 2018) is an ongoing mapping survey aims to map a portion of the first Galactic quadrant ($l = 10^\circ\text{--}40^\circ$, $|b| < 0.4^\circ$) using the Green Bank Telescope (GBT). We retrieved NH_3 (1,1) and (2,2) spectral cubes from the RAMPS pilot data release¹, which have mapped about 6.5 square degrees in a series of ten fields centered at $l = 10^\circ, 23^\circ, 24^\circ, 28^\circ, 29^\circ, 30^\circ, 31^\circ, 38^\circ, 45^\circ$ and 47° (Hogge et al. 2018). The NH_3 spectral images have a FWHM beam of about $32''$, and the rms noise is about 0.16 K at a spectral resolution of 0.2 km s^{-1} . Figure 1 shows an overview of the NH_3 emission compared to multi-wavelength images of a typical HMSC.

¹ <http://sites.bu.edu/ramps>

The RAMPS pilot surveyed area covered 51 of the 463 HMSCs distributed in the inner Galactic plane (Yuan et al. 2017). We extracted the mean spectra of each of the HMSCs within the elliptical sizes provided by Yuan et al. (2017). All the 51 HMSCs are detected in NH_3 , demonstrating the robustness of the source selection and high quality of the RAMPS data.

We fitted the NH_3 (1,1) and (2,2) spectra simultaneously using Pysepckit (Ginsburg et al. 2022), in a similar way as in (Wang et al. 2014; Sokolov et al. 2018; Wang & Wang 2023). In the process of building the fitting program, we referenced some codes from Lu et al. (2014), which uses a modular architecture to facilitate single-component and two-component fitting. The procedure models the NH_3 spectra with five free parameters: centroid velocity V_{LSR} , rotation temperature T_{rot} , NH_3 column density N_{NH_3} , line width in dispersion σ , and optical depth τ . We also added beam filling factor as a free parameter. Among the 51 clumps, 7 show more than one velocity component in the spectra. We have removed them from further analysis, and focus on the 44 HMSCs with a single velocity component in this work. The 44 HMSCs represent properties of the full sample of 463 HMSCs. Figure 2 presents an example for the fitting.

3. THERMODYNAMIC ANALYSIS

3.1. Derivation of thermal and dynamical parameters

The NH_3 fitted parameters are used together with clump mass and size from Yuan et al. (2017) for thermodynamic analysis of the HMSCs.

The rotational temperature T_{rot} governs the level population of the NH_3 system; it is related to kinetic temperature with collision coefficients. We use the empirical relationship² deduced in Walsley & Ungerechts (1983); Tafalla et al. (2004) to

² Estalella (2017) present a slightly modified relationship. For the minimum, median, and maximum T_{kin} in Table 1, the modified version differs from Equation 1 by 0.7%, 1.8%, and 4.5%, respectively.

derive T_{kin} from T_{rot} :

$$T_{\text{rot}} = \frac{T_{\text{kin}}}{1 + \frac{T_{\text{kin}}}{41.5} \ln[1 + 0.6 \exp(-\frac{15.7}{T_{\text{kin}}})]} \quad (1)$$

The line velocity dispersion is broadened due to the spectral resolution of $\Delta v_{\text{chan}} = 0.2 \text{ km s}^{-1}$. We subtract this minor broadening in quadrature

$$\sigma_v^2 = \sigma^2 - \frac{\Delta v_r^2}{8 \ln 2} \quad (2)$$

For comparison with literature, FWHM linewidth is used more frequently than velocity dispersion. For a Gaussian profile as modeled in our work and widely used in literature, one have

$$\begin{aligned} \Delta V_{\text{FWHM}} &= 2\sqrt{2\ln 2} \times \sigma_v \\ &= 2.355\sigma_v \end{aligned} \quad (3)$$

With the gas temperature determined, the thermal broadening to velocity dispersion is

$$\sigma_{\text{th}} = \sqrt{\frac{k_B T_{\text{kin}}}{m_{\text{NH}_3}}} \quad (4)$$

where k_B is the Boltzmann constant, T_{kin} is the kinetic temperature, $m_{\text{NH}_3} = 17m_{\text{H}}$ is the mass of the NH_3 molecule, m_{H} is the mass of the hydrogen atom.

The velocity dispersion due to non-thermal gas motion is then computed by subtracting that of the thermal motion in quadrature (Myers 1983; Fuller & Myers 1992)

$$\sigma_{\text{nth}} = \sqrt{\sigma_v^2 - \sigma_{\text{th}}^2} \quad (5)$$

The sonic Mach number, defined as the non-thermal velocity dispersion with respect to sound speed c_s , is then calculated as (e.g., Palau et al. 2015)

$$\begin{aligned} \mathcal{M}_S &= \frac{\sigma_{\text{nth}}}{c_s} \\ &= \frac{\sigma_{\text{nth}}}{\sqrt{(k_B T_{\text{kin}})/(\mu_m m_{\text{H}})}} \end{aligned} \quad (6)$$

where $\mu = 2.33$ is the mean molecular weight.

Then we calculate virial mass and virial parameter to assess the dynamical state of the clumps, following MacLaren et al. (1988); Bertoldi & McKee (1992):

$$\begin{aligned} M_{\text{vir}} &= 3k_1 \frac{R\sigma_v^2}{G} \\ &= 126k_1 \left(\frac{R}{\text{pc}} \right) \left(\frac{\Delta V_{\text{FWHM}}}{\text{km} \cdot \text{s}^{-1}} \right)^2 M_{\odot} \end{aligned} \quad (7)$$

where $k_1 = (5 - 2n)/(3 - n)$ is a correction factor to account for nonuniform density distribution, which is characterized by a power law profile $\rho \propto r^{-n}$. R is the equivalent radius of the clump, and G is the gravitational constant. According to observed density profiles in high-mass star formation clumps, we adopt $n = 1.8$ following Sanhueza et al. (2017), leading to $k_1 = 1.667$.

The virial parameter, defined as the ratio of the kinetic energy and gravitational energy, is then computed as

$$\alpha_{\text{vir}} = k_2 \frac{M_{\text{vir}}}{M_{\text{cl}}} \quad (8)$$

where M_{cl} is the clump mass, and k_2 is a correction factor to account for the clump's deviation from a sphere. Bertoldi & McKee (1992) derived that k_2 depends only on the clump's aspect ratio, and for the ellipticity of the HMSCs considered here (Yuan et al. 2017), k_2 equals to unity within a few percent (see Eq. A8 and Fig 2 in Bertoldi & McKee 1992; cf. Henshaw et al. 2016).

The uncertainty in α_{vir} mainly originates from uncertainties in source kinematic distance, dust emissivity, gas-to-mass ratio, NH_3 linewidth and kinetic temperature (Figure 2). Following a comprehensive uncertainty evaluation in Sanhueza et al. (2017), we quote a typical 75% uncertainty in α_{vir} .

The above derivations have neglected external pressure. Since the HMSCs are embedded within larger clouds, external pressure help to confine the clumps, and in term contribute to virial equilibrium. It has been shown that the surface energy term is of the same order as volume energy

term (Ballesteros-Paredes 2006; Dib et al. 2007). Therefore, we follow Kauffmann et al. (2013) and treat $\alpha_{\text{vir}} < 2$ as gravitationally bound, instead of $\alpha_{\text{vir}} < 1$ as the criterion.

3.2. Estimated magnetic fields

The above calculations have not considered magnetic fields, which is commonly observed in star formation regions (Liu et al. 2022; Pattle et al. 2023). Magnetic fields provide additional support against gravity. The Alfvénic turbulence is formulated as (Bertoldi & McKee 1992; Pillai et al. 2011)

$$\sigma_A = B(\mu_0 \rho)^{-\frac{1}{2}} \quad (9)$$

where ρ is the density, B is the magnetic field strength, and μ_0 is the permeability of free space. The Alfvén velocity contributes to the magnetic virial parameter as

$$\alpha_{B,\text{vir}} = \frac{3k_1 k_2 R}{GM_{\text{cl}}} \left(\sigma_v^2 + \frac{\sigma_A^2}{6} \right) \quad (10)$$

For clumps with $\alpha_{\text{vir}} < 2$, we can estimate the magnetic field strength needed to have $\alpha_{B,\text{vir}} = 2$, as adapted from Bertoldi & McKee (1992); Pillai et al. (2011); Huang et al. (2023):

$$B = \sqrt{6\mu_0\rho \left(\frac{\alpha_{B,\text{vir}} GM_{\text{cl}}}{3k_1 k_2 R} - \sigma_v^2 \right)}. \quad (11)$$

4. RESULTS AND DISCUSSION

4.1. Overall properties and Mach numbers

Table 1 lists physical properties of the HMSCs, including basic, fitted, and derived parameters, along with simple statistics. Figure 3 illustrates the parameters.

Median values of selected parameters are: clump mass $593 M_\odot$, equivalent radius 0.56 pc , molecular hydrogen number density $1.42 \times 10^4 \text{ cm}^{-3}$, kinetic temperature 16.3 K , velocity dispersion 0.76 km s^{-1} , Mach number 3.32 , virial parameter 0.32 , estimated magnetic field strength 0.39 mG , and NH_3 abundance 1.47×10^{-7} . The median values represent typical properties of the 44 HMSCs.

The Mach numbers show supersonic non-thermal motions at clump scales, but most HMSCs have $\mathcal{M}_S < 5$, inconsistent to what have been considered in some theoretical works (Sect. 1).

4.2. Correlation matrix

We explore possible correlations and trends in the parameters by building a matrix of correlation coefficients in Figure 4a.³ Strong correlations are observed in three pairs of parameters:

1. estimated magnetic field strength B_{est} and volume density n_{H_2} (correlation coefficient $P = 0.93$);
2. velocity dispersion σ_v and Mach number \mathcal{M}_S ($P = 0.93$);
3. dust temperature T_{dust} and luminosity-to-mass ratio L/M ($P = 0.92$).

The $B - n$ correlation is expected theoretically (Crutcher et al. 2010), and the $B_{\text{est}} - n_{\text{H}_2}$ correlation has been reported in Huang et al. (2023) with a weaker P . B_{est} also tends to be stronger in smaller clumps ($P = -0.53$), motivating interferometric observations for high resolution dust polarization (Liu et al. 2022; Beuther et al. 2024; Zhang et al. 2014). The $B_{\text{est}} - n_{\text{H}_2}$ correlation can be fitted in Equation 12 (Figure 4b). See more discussion in Sect. 4.3. The $T_{\text{dust}} - L/M$ correlation has been shown in Elia & Pezzuto (2016) analytically, and has also been observed by Huang et al. (2023) in a sample of 207 HMSCs. The $\sigma_v - \mathcal{M}_S$ correlation is evident in Equation 6, with little span in sound speed in these HMSCs.

Figure 4a also reveals no clear correlation in a few notable pairs of parameters. Firstly, the dust and gas temperature are not well correlated, although the difference among the two are mostly $< 5 \text{ K}$ (Figure 4c). Gas temperature has a larger

³ To efficiently read the matrix (Figure 4a), for example, for B_{est} , first start with B_{est} on the left column and move to rightmost, then turn down to move vertically.

dynamical range (10.9–29.5 K) than dust temperature (10.6–20.3 K), as have been pointed out in Wang (2018). Poor correlation between dust and gas temperature further necessitates temperature derived using spectral lines with radial velocity corresponding to the source’s emission, to avoid line-of-sight contamination. Yuan et al. (2017) have already subtracted a modeled background/foreground before fitting SED. Still, our results show that spectral line derived gas temperature is necessary to better constrain the temperature. See more discussion on T_{dust} and T_{kin} in Wang (2018); Merello et al. (2019). Secondly, clump radii do not show clear correlation with Mach number or velocity dispersion, although positive trends ($P > 0$) are evident. It is known that turbulence dissipates from large to small scales in a given molecular cloud (e.g. Wang et al. 2008; Yue et al. 2021). The observational results here indicate that turbulence can be different from one source to another, and multi-scale observations in individual sources are needed to further investigate the dissipation of turbulence over spatial scales (Liu et al. 2024). Thirdly, NH_3 fractional abundance does not appear to correlate with evolutionary indicators like L/M and temperature, suggesting that NH_3 abundance is stable in the initial stages as in HMSCs. Lastly, the linewidth-size relation (Larson 1981) does not hold in scales smaller than $\lesssim 1$ pc, as already found in a number of observations (e.g. Wang et al. 2009; Huang et al. 2023). Notably, some of the non-correlations may be partly affected by narrow ranges of parameters, as the HMSCs are strictly selected to be starless. This needs to be taken into account particularly when comparing these (non-)correlations with those derived from clumps in a wider evolutionary stages, and therefore occupying larger parameter ranges.

4.3. Sub-virial clumps and implications

The most intriguing finding is the small α_{vir} , which is in range 0.13–1.37 except an outlier at 3.31 (G030.7912–0.1173). The outlier source has a marginal detection in NH_3 (2,2), and the fitted

line velocity dispersion is $\sigma = 1.72 \pm 0.48 \text{ km s}^{-1}$, with a large uncertainty compared to other sources. So, all but one of the 44 HMSCs have $\alpha_{\text{vir}} < 2$ (40 of them have $\alpha_{\text{vir}} < 1$), suggesting that internal kinetic energy is insufficient to support HMSCs against from gravitational collapse. Similarly small virial parameters have been reported by Merello et al. (2019) in a comparative study by cross-matching HiGAL clumps to literature NH_3 studies. Unlike the uniform RAMPS data, the literature data have diverse sky coverages and various spectral resolution, some of which are larger than sound speed. In a classic Effelsberg NH_3 study of IRDCs, Pillai et al. (2006) find $\alpha_{\text{vir}} \sim 1$.

Kauffmann et al. (2013) compiled and standardized from the literature 1325 virial parameter estimates on a range of cloud structures, from clouds, clumps, to cores. They reported low virial parameters of $\ll 2$ in some high-mass star formation regions, mostly from the ATLASGAL clumps of Wienen et al. (2012). A close inspection of their Fig. 1 finds that our virial parameters (median 0.32, mostly less than 0.7) populate the lower end of the Wienen et al. (2012) virial parameters. This is reasonable, because most of the Wienen et al. (2012) clumps are of protostellar nature (see Introduction), and star formation activity within the clumps have broadened the initial linewidth.

In order to stabilize the 43 HMSCs with $\alpha_{\text{vir}} < 2$, magnetic fields with strength of 0.10–2.65 mG (median 0.39 mG) would be needed (Table 1). We compare the estimated strengths to that derived from observations at the clump scales. Liu et al. (2018) present JCMT 850 μm dust polarization observations towards a well characterized filamentary IRDC G035.39–00.33 (e.g., Jiménez-Serra et al. 2010; Henshaw et al. 2016; Sokolov et al. 2017, 2018, 2019). At a resolution of 14'' (0.18 pc), the observations measure a mean plane-of-the-sky magnetic field strength of ~ 0.05 mG, much lower than B_{est} in the HMSCs even assuming a similar line-of-sight strength. The 6.8 pc main filament as a whole is gravitationally unstable if it is only sup-

ported by thermal pressure and turbulence; adding the magnetic support can stabilize the northern part of the filament, but not the southern and central parts. Nine clumps are distributed along the filament, with mass $35\text{--}219 M_{\odot}$, effective radii 0.12–0.31 pc, and B_{clump} 0.056–0.219 mG. The clumps are similar to the smallest HMSCs in Table 1, and the observed B-field strengths are among the smallest compared to B_{est} . Considering that B_{est} tends to become stronger in smaller HMSCs ($P = -0.53$, Figure 4a), the required B_{est} to stabilize HMSCs would be strong compared to the observations in G035.39-00.33.

Liu et al. (2022) compiled 288 polarized dust emission observations from the literature and recalculated the total magnetic field strength using a revised Davis-Chandrasekhar-Fermi (DCF) method. In a classic $B-n$ plot (Figure 4b), the 288 measurements are compared with the estimated B-field strength in the 43 HMSCs. The B_{est} are systematically higher than observed strength in the same density range. The B_{est} shows a tight correlation with density, which can be fitted as

$$B_{\text{mG}} = 0.269 n_4^{0.61} \quad (12)$$

where B_{mG} is B in units of mG and n_4 is n_{H_2} in 10^4 cm^{-3} . Liu et al. (2022) fitted $B_{\text{mG}} = 0.059 n_4^{0.57}$ for polarized dust measurements, and Crutcher et al. (2010) fitted $B_{\text{mG}} = 0.098 n_4^{0.65}$ for Zeeman splitting measurements (at $n_{\text{H}_2} > 300 \text{ cm}^{-3}$). The power-law indices are similar but the strengths are different. For the typical density of $1.42 \times 10^4 \text{ cm}^{-3}$ of the HMSCs, B_{est} is 4.6 and 2.7 times that of the polarized dust measurements and Zeeman splitting measurements, respectively. It is important to note that the B observations are mainly from star formation regions at later evolutionary stages than HMSCs. Observations towards the initial stages (e.g. Liu et al. 2018) are very rare so far.

The results suggest that global dynamic collapse at clump scale is common, which is widely observed in massive clumps with global infall signatures (He et al. 2015, 2016; Yu et al. 2022; Xu

et al. 2023a) and resolved multiscale gas flows (e.g., Yuan et al. 2018; Zhou et al. 2022; Zhang et al. 2023; Xu et al. 2023b).

The implications of these findings are two folds. Observationally, constraints on the *initial* conditions of massive star formation have finally reached a Galaxy-wide sense, to a pilot yet representative sample of 44 HMSCs built on our previous work (Yuan et al. 2017; Huang et al. 2023). These HMSCs represent the very first observed physical properties that are important to refine the initial inputs to theoretical models. Theoretically, the prevalence of sub-virial clumps (radii 0.13–1.12 pc, Table 1) is in stark contrast to the virial equilibrium assumed in the turbulent core model (Sect. 1). Note that in this model both cores and clumps are assumed to be in virial equilibrium, based on limited observational constraints available at that time (see more details in McKee & Tan 2003). This assumption only applies to the initial conditions, i.e., starless/prestellar stage, not protostellar stage (McKee & Tan 2003). Sub-virial presteallar and protostellar cores (smaller than most of the HMSCs) have been reported (e.g., Zhang et al. 2015; Sanhueza et al. 2017; Liu et al. 2020; Barnes et al. 2021; Li et al. 2023; Jiao et al. 2023). The findings in this work are drawn from a systematic characterization using uniform data on a uniform sample of HMSCs, providing the first statistically significant constraints on the *initial* conditions. The HMSCs are therefore of great interest for follow-up observations at high-resolution, to resolve the beginning of star formation (e.g., Jiao et al. 2023, for G010.2144-0.3051).

The findings urge future observations to quantify the support of magnetic fields in the initial, starless stages of massive star formation regions, like the HMSCs well characterized here. Although challenging to observe, dust polarization imaging by JCMT, SOFIA, SMA, and ALMA has recently been carried out toward massive clumps bright at sub-millimeter, mostly at a later evolutionary stage than HMSCs (e.g. Zhang et al. 2014; Beuther et al.

2024; Sanhueza et al. 2021; Stephens et al. 2022; Liu et al. 2022; Pattle et al. 2023). It would be even more challenging to do so for HMSCs because they are generally less bright. If the B-field strengths in HMSCs are indeed as strong as B_{est} in Figure 4(b), observations may be less time consuming than previously thought. Alternatively, velocity fields and density gradients have been proposed to indirectly probe magnetic fields (e.g., Jiao et al. 2024b). The only direct measurement of the magnetic field strength relies on observing Zeeman splitting (Crutcher et al. 2010; Crutcher 2012). Recently, Ching et al. (2022) have demonstrated the feasibility of using HI narrow self-absorption (HINSA) to measure Zeeman splitting with FAST. Several well-characterized HMSCs here can be targets for such exciting experiments in the FAST era, which we are carrying out (Sun et al. 2024).

The huge difference between the estimated B-field strengths needed to stabilize starless clumps and that observed in protostellar and more evolved clumps strongly suggests a dynamical star formation initiated by collapsing, not equilibrium, clumps. Without sufficient support from magnetic fields, the collapse would be very quick, nearly free-fall, resulting in short lifetime of the high-mass starless cores in the framework of the turbulent core model (Kauffmann et al. 2013). This is consistent with the very few numbers of observed high-mass starless cores after decades of searching (e.g., Bontemps et al. 2010; Wang et al. 2014; Motte et al. 2018; Jiao et al. 2023, 2024a; Barnes et al. 2023).

5. CONCLUSIONS

Built on our previous Galaxy-wide characterization of \sim pc scale high-mass starless clumps (HMSCs), here we have investigated the dynamical state of a representative subsample of 44 HMSCs, aiming to reveal the initial conditions for high-mass star formation. The main findings and implications are as follows.

(1) By modeling GBT NH₃ (1,1) and (2,2) spectra extracted from each of the HMSCs, we de-

rived line velocity dispersion (range 0.48–1.72, median 0.76 km s⁻¹), gas kinetic temperature (range 10.9–29.5, median 16.3 K), NH₃ column density ($1.23 \times 10^{-8} – 3.37 \times 10^{-7}$, median 1.47×10^{-7}), Mach number (1.80–7.36, median 3.32, mostly < 5), and virial parameter (range 0.13–1.37, median 0.32, and an outlier at 3.31).

(2) The Mach numbers show that these HMSCs have supersonic turbulence, but most of them have M_S lower than 5, inconsistent to what have been considered in some theoretical works (Sect. 1).

(3) Thermodynamic analysis reveals that all but one (43/44) of the HMSCs are gravitationally bound with virial parameter $\alpha_{\text{vir}} < 2$. In order to balance these HMSCs from gravity, as suggested in the turbulent core model, the estimated B-field strength correlates tightly with density, $B_{\text{est}}/\text{mG} = 0.269 (n_{\text{H}_2}/10^4 \text{ cm}^{-3})^{0.61}$, with a similar power-law index as found in previous dust polarization observations, but a factor of 4.6 higher in strength.

(4) For the first time, the initial dynamical state of high-mass formation regions has been constrained to be sub-virial in a statistically significance manner with uniform data and sample. This is in contradictory to theoretical models in virial equilibrium, while in agreement with recent observations revealing a dynamic, not quasi-static, massive protocluster formation, and consistent with the lack of observed high-mass starless cores.

(5) The findings urge future observations to quantify the magnetic field support in the prestellar stage of massive clumps, which are rarely explored so far, towards a full understanding of the physical conditions that initiate massive star formation. The Five-hundred-meter Aperture Spherical radio Telescope (FAST) can make a significant contribution with demonstrated Zeeman splitting observations of HINSA, to directly measure magnetic field strength.

The HMSCs well characterized here represent the very first observed properties that would initiate massive star formation, if not already. These

properties should be accounted in theoretical explorations. Further ALMA observations are ongoing to resolve the beginning of massive star formation within these HMSCs (e.g., Jiao et al. 2023).

1 We thank the referee for in-depth evaluation and
2 constructive suggestions that helped strengthen the
3 original manuscript. We acknowledge support
4 from the National Natural Science Foundation of
5 China (12041305, 12033005), the Tianchi Talent
6 Program of Xinjiang Uygur Autonomous Region,
7 the China-Chile Joint Research Fund (CCJRF No.
8 2211), and the High-Performance Computing Plat-
9 form of Peking University. CCJRF is provided
10 by Chinese Academy of Sciences South Amer-
11 ica Center for Astronomy (CASSACA) and es-
12 tablished by National Astronomical Observato-
13 ries, Chinese Academy of Sciences (NAOC) and
14 Chilean Astronomy Society (SOCHIAS) to sup-
15 port China-Chile collaborations in astronomy. This
16 publication makes use of molecular line data from
17 the Radio Ammonia Mid-Plane Survey (RAMPS).
18 RAMPS is supported by the National Science
19 Foundation under grant AST-1616635. The Green
20 Bank Observatory is a facility of the National Sci-
21 ence Foundation operated under cooperative agree-
22 ment by Associated Universities, Inc.

Table 1. Physical Properties of the 44 HMSCs

Name	RA deg	Dec deg	V_{LSR} km s ⁻¹	d kpc	T_{kin} K	σ_v km s ⁻¹	ΔV_{FWHM} km s ⁻¹	N_{NH_3}	\mathcal{M}_S	α_{vir}	B_{est}	T_{dust}	M_{cl}	L/M	R	N_{H_2} pc cm ⁻²	χ_{NH_3}	n_{H_2} cm ⁻³
(1)	(2)	(3)	(4)	(5)	(6)	(7)	(8)	(9)	(10)	(11)	(12)	(13)	(14)	(15)	(16)	(17)	(18)	(19)
G009.9517-0.3649	272.2560	-20.5094	13.0	3.12	14.8	0.51	1.21	5.67E+15	2.21	0.29	12.0	2.65E+02	0.33	0.36	4.82E+22	1.18E-07	1.91E+04	
G010.1904-0.3884	272.4012	-20.3118	10.9	3.12	20.9	0.93	2.18	1.21E+16	3.38	0.61	0.61	18.9	3.15E+02	4.48	0.28	6.34E+22	1.91E-07	5.21E+04
G010.1976-0.2876	272.3108	-20.2568	10.5	3.12	15.2	0.51	1.21	4.74E+15	2.18	0.22	0.65	18.0	2.15E+02	2.67	0.22	4.01E+22	1.18E-07	6.97E+04
G010.2144-0.3051	272.3358	-20.2506	12.0	3.12	17.6	0.88	2.06	1.43E+16	3.49	0.27	2.65	16.6	2.96E+02	2.26	0.13	6.21E+22	2.30E-07	4.89E+05
G010.2190-0.3632	272.3924	-20.2746	12.0	3.12	20.5	0.99	2.32	8.46E+15	3.64	0.73	0.51	18.4	3.33E+02	3.67	0.31	6.26E+22	1.35E-07	3.94E+04
G010.2488-0.1101	272.1718	-20.1259	14.2	14.56	18.5	1.01	2.37	7.39E+15	3.92	0.20	0.53	16.8	4.57E+03	2.25	1.12	3.90E+22	1.89E-07	1.12E+04
G022.5309-0.1927	278.2485	-9.3350	76.6	4.98	16.7	0.95	2.23	8.26E+15	3.87	0.66	0.28	12.4	6.56E+02	0.48	0.59	3.85E+22	2.14E-07	1.10E+04
G022.7215-0.2733	278.4099	-9.2032	73.4	4.64	16.7	0.50	1.18	3.48E+15	2.04	0.21	0.24	16.3	5.79E+02	2.03	0.60	3.69E+22	9.43E-08	9.29E+03
G023.2674-0.3559	278.7389	-8.7567	77.2	4.52	12.3	1.54	3.62	7.66E+15	7.36	1.08	0.86	14.3	5.39E+02	0.65	0.30	4.49E+22	1.71E-07	6.66E+04
G023.2694-0.2097	278.6085	-8.6876	78.9	4.74	15.8	0.82	1.92	8.25E+15	3.43	0.29	0.48	11.8	1.08E+03	0.31	0.57	7.39E+22	1.12E-07	1.98E+04
G023.2778-0.2149	278.6171	-8.6826	78.4	4.89	14.6	1.02	2.39	1.10E+16	4.46	0.30	0.93	11.5	1.20E+03	0.25	0.43	9.14E+22	1.20E-07	5.07E+04
G023.2826-0.2007	278.6066	-8.6718	79.8	4.83	16.3	1.13	2.65	1.06E+16	4.68	0.67	0.35	10.7	1.00E+03	0.20	0.65	7.61E+22	1.39E-07	1.27E+04
G023.2957-0.0556	278.3827	-8.5420	55.5	3.63	11.4	0.91	2.13	7.34E+15	4.50	0.60	0.51	11.4	3.55E+02	0.21	0.32	4.52E+22	1.62E-07	3.72E+04
G023.2989-0.2501	278.66801	82.7	5.44	16.5	0.61	1.45	6.15E+15	2.51	0.13	1.85	14.1	4.52E+02	0.90	0.19	3.03E+22	2.03E-07	2.31E+05	
G023.3222-0.0775	278.5145	-8.5799	97.1	5.82	14.0	0.74	1.73	6.00E+15	3.28	0.27	0.52	13.7	7.63E+02	0.62	0.46	4.17E+22	1.44E-07	2.62E+04
G023.4556-0.2301	278.7135	-8.5317	103.6	5.93	15.3	0.48	1.14	3.51E+15	2.04	0.19	0.20	20.3	7.05E+02	5.98	0.72	2.72E+22	1.29E-07	6.45E+03
G023.4742-0.1037	278.4227	-8.3614	87.0	5.57	16.8	1.00	2.35	1.04E+16	4.07	0.34	0.78	14.1	1.05E+03	0.94	0.44	6.08E+22	1.71E-07	4.14E+04
G023.4771-0.1147	278.4142	-8.3538	87.6	5.56	16.3	0.74	1.73	6.76E+15	3.04	0.20	0.75	12.2	9.16E+02	0.40	0.42	5.47E+22	1.24E-07	4.14E+04
G023.5176-0.2425	278.3185	-8.2589	82.4	5.40	15.5	0.64	1.52	1.90E+15	2.73	0.32	0.48	17.9	3.39E+02	2.74	0.32	2.15E+22	8.85E-08	3.49E+04
G023.9790-0.1498	278.6164	-7.8922	82.3	4.43	15.7	0.66	1.57	5.92E+15	2.79	0.32	0.42	15.7	4.37E+02	1.57	0.39	4.10E+22	1.44E-07	2.52E+04
G024.0179-0.2107	278.5800	-7.8296	106.5	5.98	15.3	0.88	2.06	5.21E+15	3.75	0.51	0.22	14.9	1.02E+03	1.08	0.82	4.20E+22	1.24E-07	6.25E+03
G024.0492-0.2145	278.9756	-7.9976	81.6	4.80	12.7	0.72	1.68	5.08E+15	3.35	0.57	0.17	12.7	4.53E+02	0.47	0.62	3.40E+22	1.49E-07	6.52E+03
G024.2583-0.1022	278.7889	-7.6662	99.7	5.89	16.7	0.55	1.30	5.19E+15	2.25	0.31	0.25	12.3	3.79E+02	0.46	0.47	2.18E+22	2.38E-07	1.27E+04
G024.4326-0.3238	278.6714	-7.4094	114.9	6.81	23.2	1.18	2.77	2.68E+15	4.09	1.37	0.15	15.2	6.63E+02	1.88	0.81	1.99E+22	1.35E-07	4.35E+03
G028.1943-0.0747	280.7620	-4.2496	98.6	8.19	14.6	0.67	1.59	5.25E+15	2.94	0.17	0.38	15.3	1.83E+03	1.16	0.84	5.09E+22	1.03E-07	1.06E+04
G028.2726-0.1666	280.8799	-4.2219	79.9	4.50	13.5	0.93	2.18	1.06E+16	4.22	0.27	0.56	10.6	1.82E+03	0.17	0.69	9.42E+22	1.13E-07	1.90E+04
G028.5246-0.2519	281.0714	-4.0368	87.7	4.69	13.9	0.57	1.35	6.76E+15	2.56	0.20	0.67	12.8	4.08E+02	0.45	0.30	3.44E+22	1.96E-07	5.34E+04
G028.5413-0.2371	281.0658	-4.0152	86.8	4.62	14.1	0.74	1.73	5.04E+15	3.27	0.25	0.39	12.9	1.13E+03	0.45	0.65	6.77E+22	7.44E-08	1.43E+04
G029.5561-0.1861	281.1531	-2.9191	80.3	4.58	14.1	0.59	1.40	3.86E+15	2.63	0.46	0.17	12.8	3.36E+02	0.45	0.54	3.02E+22	1.28E-07	7.41E+03
G029.8406-0.0342	281.4794	-2.7665	100.2	7.67	18.8	0.74	1.73	1.47E+15	2.83	0.29	0.36	14.5	9.26E+02	1.13	0.62	2.96E+22	4.96E-08	1.36E+04

Table 1 *continued*

Table 1 (continued)

Name	RA	Dec	V_{LSR}	d	T_{kin}	σ_v	ΔV_{FWHM}	N_{NH_3}	\mathcal{M}_S	α_{vir}	B_{est}	T_{dust}	M_{cl}	L/M	R	N_{H_2}	χ_{NH_3}	n_{H_2}	
(1)	deg (2)	deg (3)	km s ⁻¹ (4)	kpc (5)	K (6)	km s ⁻¹ (7)	km s ⁻¹ (8)	(9)	(10)	(11)	mG (12)	K (13)	M_{\odot} (14)	L_{\odot}/M_{\odot} (15)	pc (16)	cm ⁻² (17)	(18)	cm ⁻³ (19)	
G030.0062-0.1192	281.6308	-2.6380	99.4	6.89	15.7	0.65	1.54	6.23E+15	2.75	0.28	0.31	13.7	7.18E+02	0.68	0.58	2.75E+22	2.27E-07	1.26E+04	
G030.0556+0.0995	281.4585	-2.5143	97.6	6.75	17.2	0.66	1.57	3.78E+15	2.67	0.38	0.23	14.6	5.59E+02	1.17	0.60	2.33E+22	1.63E-07	9.12E+03	
G030.4235-0.2142	281.9059	-2.3301	103.8	7.23	20.5	0.95	2.23	3.02E+15	3.49	0.54	0.27	17.6	1.00E+03	3.07	0.74	3.41E+22	8.86E-08	8.64E+03	
G030.5682-0.0258	281.8042	-2.1153	88.3	4.86	17.9	1.01	2.37	6.70E+15	3.98	0.70	0.40	15.0	5.02E+02	1.26	0.43	3.90E+22	1.72E-07	2.23E+04	
G030.6574+0.0446	281.7823	-2.0038	81.5	4.66	12.6	0.99	2.32	7.45E+15	4.66	0.89	0.22	14.7	5.24E+02	0.87	0.59	3.75E+22	1.99E-07	9.01E+03	
G030.6858-0.0306	281.8622	-2.0129	89.7	5.00	22.1	1.40	3.29	1.50E+16	4.98	0.66	0.39	17.9	2.23E+03	3.35	0.92	9.07E+22	1.65E-07	9.94E+03	
G030.7912-0.1173	281.9875	-1.9586	94.2	5.31	20.8	1.72	4.05	3.84E+15	6.32	3.31	15.9	3.14E+02	2.00	0.43	2.09E+22	1.83E-07	1.34E+04		
G030.7941+0.0736	281.8189	-1.8689	90.0	4.98	29.5	0.59	1.40	4.13E+15	1.80	0.75	0.11	15.6	1.93E+02	2.23	0.50	1.23E+22	3.37E-07	5.18E+03	
G030.8139-0.0235	281.9140	-1.8964	95.2	5.77	20.5	1.30	3.05	1.33E+16	4.80	0.32	1.09	19.1	2.48E+03	4.11	0.58	1.36E+23	9.78E-08	4.48E+04	
G030.8447+0.1775	281.7495	-1.7765	96.4	6.52	15.5	0.78	1.83	8.88E+15	3.29	0.29	0.38	11.0	1.08E+03	0.25	0.64	5.01E+22	1.77E-07	1.40E+04	
G030.8523-0.1086	282.0077	-1.9002	100.7	6.34	18.5	0.65	1.54	6.70E+15	2.53	0.25	0.26	17.1	1.08E+03	2.82	0.78	4.28E+22	1.57E-07	7.84E+03	
G030.8620+0.0392	281.8805	-1.8242	74.7	5.13	10.9	0.64	1.52	4.52E+15	3.26	0.33	0.34	19.4	4.49E+02	2.66	0.44	2.99E+22	1.51E-07	1.83E+04	
G030.8624+0.0394	281.9506	-1.8597	94.6	5.65	16.3	0.56	1.33	5.25E+15	2.32	0.20	0.47	17.9	5.06E+02	2.99	0.40	3.17E+22	1.65E-07	2.76E+04	
G031.1496-0.2650	281.8108	-1.4653	102.4	6.62	20.9	0.98	2.30	2.35E+14	3.57	1.24	0.10	20.0	6.07E+02	6.65	0.97	1.91E+22	1.23E-08	2.32E+03	
Min				10.5	3.12	10.9	0.48	1.14	2.35E+14	1.80	0.13	0.10	10.6	1.93E+02	0.17	0.13	1.23E+22	1.23E-08	2.32E+03
Max				114.9	14.56	29.5	1.72	4.05	1.50E+16	7.36	3.31	2.65	20.3	4.57E+03	6.65	1.12	1.36E+23	3.37E-07	4.89E+05
Median				86.9	5.07	16.3	0.76	1.78	6.08E+15	3.32	0.32	0.39	14.8	5.93E+02	1.15	0.56	3.96E+22	1.47E-07	1.42E+04
Avg				78.6	5.45	16.8	0.84	1.98	6.59E+15	3.45	0.51	0.51	15.0	8.47E+02	1.70	0.54	4.59E+22	1.50E-07	3.74E+04
Std				28.9	1.85	3.5	0.28	0.66	3.33E+15	1.12	0.52	0.46	2.70	7.73E+02	1.56	0.22	2.43E+22	5.56E-08	7.83E-04

NOTE— Col. (1) HMSC name. Col. (2-3) J2000 coordinates. Col. (4) NH₃ fitted radial velocity. Col. (5) Distance. Col. (6) kinetic temperature. Col. (7-8) velocity dispersion and FWHM linewidth. Col. (9) NH₃ column density. Col. (10-12) Derived parameters: Mach number, virial parameter, and estimated magnetic field strength. Col. (13-17) Dust temperature, clump mass, luminosity-to-mass ratio, equivalent radius, column density. Col. (18) NH₃ abundance. Col. (19) volume density.

Data for Col. (1-3, 5, 13-17, 19) are adopted or updated from Yuan et al. (2017). The NH₃ fitted V_{LSR} is consistent with that of Yuan et al. (2017), except in one source, G030.7941+0.0736. Its V_{LSR} has been updated to 90.0 km s⁻¹ according to NH₃ detection. Yuan et al. (2017) adopted 36.4 km s⁻¹ from literature. Both of the two V_{LSR} correspond to velocity components along the line of sight, and 90.0 km s⁻¹ coincides with the brightest ¹³CO (3-2) peak in the JCMT spectra (Dempsky et al. 2013). The kinematic distance is updated using $V_{\text{LSR}} = 90 \text{ km s}^{-1}$, and related parameters are updated accordingly. The derived T_{kin} is not always consistent with T_{dust} . Assuming coupling between dust and gas, and because dust temperature may suffer from line-of-sight contamination, we have updated the mass by using T_{kin} instead of the T_{dust} , in a Rayleigh-Jeans approximation, i.e., mass scales linearly with temperature.

Facilities: GBT, Spitzer, Herschel

Software: Pysepckit (Ginsburg et al. 2022)

REFERENCES

- Ballesteros-Paredes, J. 2006, Monthly Notices of the Royal Astronomical Society, 372, 443, doi: [10.1111/j.1365-2966.2006.10880.x](https://doi.org/10.1111/j.1365-2966.2006.10880.x)
- Barnes, A. T., Henshaw, J. D., Fontani, F., et al. 2021, MNRAS, 503, 4601, doi: [10.1093/mnras/stab803](https://doi.org/10.1093/mnras/stab803)
- Barnes, A. T., Liu, J., Zhang, Q., et al. 2023, A&A, 675, A53, doi: [10.1051/0004-6361/202245668](https://doi.org/10.1051/0004-6361/202245668)
- Benjamin, R. A., Churchwell, E., Babler, B. L., et al. 2003, PASP, 115, 953, doi: [10.1086/376696](https://doi.org/10.1086/376696)
- Bergin, E. A., & Tafalla, M. 2007, ARA&A, 45, 339, doi: [10.1146/annurev.astro.45.071206.100404](https://doi.org/10.1146/annurev.astro.45.071206.100404)
- Bertoldi, F., & McKee, C. F. 1992, ApJ, 395, 140, doi: [10.1086/171638](https://doi.org/10.1086/171638)
- Beuther, H., Gieser, C., Soler, J. D., et al. 2024, A&A, 682, A81, doi: [10.1051/0004-6361/202348117](https://doi.org/10.1051/0004-6361/202348117)
- Bonnell, I. A., Bate, M. R., Clarke, C. J., & Pringle, J. E. 2001, Monthly Notices of the Royal Astronomical Society, 323, 785, doi: [10.1046/j.1365-8711.2001.04270.x](https://doi.org/10.1046/j.1365-8711.2001.04270.x)
- Bontemps, S., Motte, F., Csengeri, T., & Schneider, N. 2010, A&A, 524, A18, doi: [10.1051/0004-6361/200913286](https://doi.org/10.1051/0004-6361/200913286)
- Carey, S. J., Noriega-Crespo, A., Mizuno, D. R., et al. 2009, PASP, 121, 76, doi: [10.1086/596581](https://doi.org/10.1086/596581)
- Chen, H.-R., Liu, S.-Y., Su, Y.-N., & Zhang, Q. 2010, ApJL, 713, L50, doi: [10.1088/2041-8205/713/1/L50](https://doi.org/10.1088/2041-8205/713/1/L50)
- Ching, T. C., Li, D., Heiles, C., et al. 2022, Nature, 601, 49, doi: [10.1038/s41586-021-04159-x](https://doi.org/10.1038/s41586-021-04159-x)
- Crutcher, R. M. 2012, ARA&A, 50, 29, doi: [10.1146/annurev-astro-081811-125514](https://doi.org/10.1146/annurev-astro-081811-125514)
- Crutcher, R. M., Wandelt, B., Heiles, C., Falgarone, E., & Troland, T. H. 2010, ApJ, 725, 466, doi: [10.1088/0004-637X/725/1/466](https://doi.org/10.1088/0004-637X/725/1/466)
- Csengeri, T., Urquhart, J. S., Schuller, F., et al. 2014, A&A, 565, A75, doi: [10.1051/0004-6361/201322434](https://doi.org/10.1051/0004-6361/201322434)
- Cyganowski, C. J., Illee, J. D., Brogan, C. L., et al. 2022, ApJL, 931, L31, doi: [10.3847/2041-8213/ac69ca](https://doi.org/10.3847/2041-8213/ac69ca)
- Dempsey, J. T., Thomas, H. S., & Currie, M. J. 2013, ApJS, 209, 8, doi: [10.1088/0067-0049/209/1/8](https://doi.org/10.1088/0067-0049/209/1/8)
- Dib, S., Kim, J., Vázquez-Semadeni, E., Burkert, A., & Shadmehri, M. 2007, ApJ, 661, 262, doi: [10.1086/513708](https://doi.org/10.1086/513708)
- Duarte-Cabral, A., Colombo, D., Urquhart, J. S., et al. 2021, The SEDIGISM survey: molecular clouds in the inner Galaxy, OUP, doi: [10.1093/mnras/staa2480](https://doi.org/10.1093/mnras/staa2480)
- Elia, D., & Pezzuto, S. 2016, Monthly Notices of the Royal Astronomical Society, 461, 1328
- Estalella, R. 2017, PASP, 129, 025003, doi: [10.1088/1538-3873/129/972/025003](https://doi.org/10.1088/1538-3873/129/972/025003)
- Federrath, C., & Klessen, R. S. 2012, ApJ, 761, 156, doi: [10.1088/0004-637X/761/2/156](https://doi.org/10.1088/0004-637X/761/2/156)
- Feng, S., Beuther, H., Zhang, Q., et al. 2016, ApJ, 828, 100, doi: [10.3847/0004-637X/828/2/100](https://doi.org/10.3847/0004-637X/828/2/100)
- Fuller, G. A., & Myers, P. C. 1992, ApJ, 384, 523, doi: [10.1086/170894](https://doi.org/10.1086/170894)
- Ginsburg, A., Sokolov, V., de Val-Borro, M., et al. 2022, AJ, 163, 291, doi: [10.3847/1538-3881/ac695a](https://doi.org/10.3847/1538-3881/ac695a)
- Goldsmith, P. F. 2001, ApJ, 557, 736, doi: [10.1086/322255](https://doi.org/10.1086/322255)
- He, Y.-X., Zhou, J.-J., Esimbek, J., et al. 2015, MNRAS, 450, 1926, doi: [10.1093/mnras/stv732](https://doi.org/10.1093/mnras/stv732)
- . 2016, MNRAS, 461, 2288, doi: [10.1093/mnras/stw1301](https://doi.org/10.1093/mnras/stw1301)
- Henshaw, J. D., Caselli, P., Fontani, F., et al. 2016, MNRAS, 463, 146, doi: [10.1093/mnras/stw1794](https://doi.org/10.1093/mnras/stw1794)
- Ho, P. T. P., & Townes, C. H. 1983, ARA&A, 21, 239, doi: [10.1146/annurev.aa.21.090183.001323](https://doi.org/10.1146/annurev.aa.21.090183.001323)
- Hogge, T., Jackson, J., Stephens, I., et al. 2018, ApJS, 237, 27, doi: [10.3847/1538-4365/aacf94](https://doi.org/10.3847/1538-4365/aacf94)
- Huang, B., Wang, K., Girart, J. M., et al. 2023, The Astrophysical Journal, 949, 46, doi: [10.3847/1538-4357/acc532](https://doi.org/10.3847/1538-4357/acc532)
- Jiao, W., Wang, K., Pillai, T. G. S., et al. 2023, ApJ, 945, 81, doi: [10.3847/1538-4357/acb211](https://doi.org/10.3847/1538-4357/acb211)
- Jiao, W., Wang, K., & Xu, F. 2024a, AJ, 168, 151, doi: [10.3847/1538-3881/ad6dda](https://doi.org/10.3847/1538-3881/ad6dda)
- Jiao, W., Wang, K., Xu, F., Wang, C., & Beuther, H. 2024b, A&A, 686, A202, doi: [10.1051/0004-6361/202449182](https://doi.org/10.1051/0004-6361/202449182)
- Jiménez-Serra, I., Caselli, P., Tan, J. C., et al. 2010, MNRAS, 406, 187, doi: [10.1111/j.1365-2966.2010.16698.x](https://doi.org/10.1111/j.1365-2966.2010.16698.x)
- Kauffmann, J., Pillai, T., & Goldsmith, P. F. 2013, ApJ, 779, 185, doi: [10.1088/0004-637X/779/2/185](https://doi.org/10.1088/0004-637X/779/2/185)
- Krumholz, M. R., Klein, R. I., & McKee, C. F. 2007a, ApJ, 656, 959, doi: [10.1086/510664](https://doi.org/10.1086/510664)
- . 2007b, ApJ, 665, 478, doi: [10.1086/519305](https://doi.org/10.1086/519305)

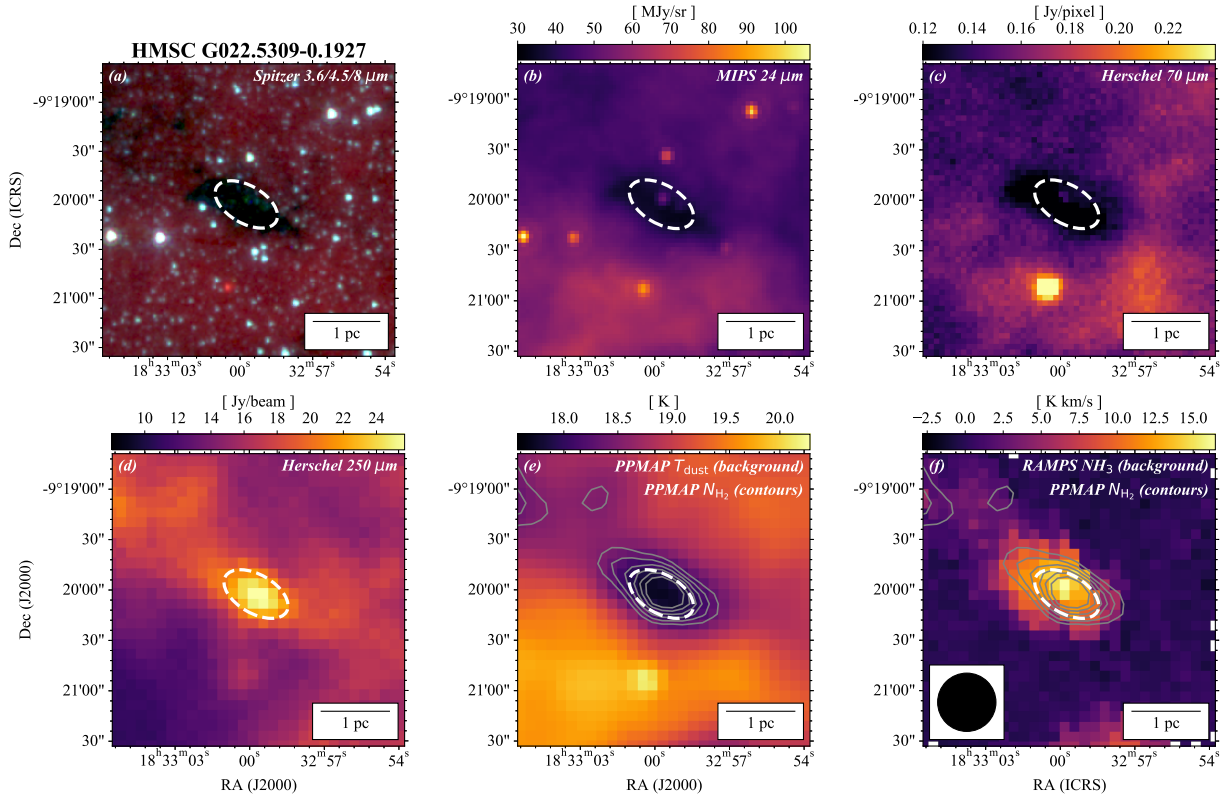


Figure 1. Overview of an example high-mass starless clump (HMSC) G022.5309-0.1927. (a) Three pseudo-color images with *Spitzer* maps at 8.0, 4.5, and 3.6 μm (Benjamin et al. 2003) rendered in red, green, and blue, respectively. (b) *Spitzer* 24 μm emission (Carey et al. 2009). (c) *Herschel* 70 μm emission (Molinari et al. 2010, 2016b). (d) *Herschel* 250 μm emission. (e) the dust temperature is shown in background and H_2 column density in gray contours of [2.0, 2.5, 3.0, 3.5, 4.0, 4.5, 5.0] $\times 10^{22} \text{ cm}^{-2}$ (Marsh et al. 2017). (f) moment 0 map of $\text{NH}_3(1,1)$ data of RAMPS show a good spatial correlation with cold dust emission; the GBT beam size is shown at the bottom left corner. In all panels, the white dashed ellipse outlines the source size.

- Larson, R. B. 1981, Monthly Notices of the Royal Astronomical Society, 194, 809, doi: [10.1093/mnras/194.4.809](https://doi.org/10.1093/mnras/194.4.809)
- Li, S., Sanhueza, P., Zhang, Q., et al. 2023, ApJ, 949, 109, doi: [10.3847/1538-4357/acc58f](https://doi.org/10.3847/1538-4357/acc58f)
- Liu, J., Qiu, K., & Zhang, Q. 2022, ApJ, 925, 30, doi: [10.3847/1538-4357/ac3911](https://doi.org/10.3847/1538-4357/ac3911)
- Liu, J., Zhang, Q., Qiu, K., et al. 2020, ApJ, 895, 142, doi: [10.3847/1538-4357/ab9087](https://doi.org/10.3847/1538-4357/ab9087)
- Liu, J., Zhang, Q., Lin, Y., et al. 2024, ApJ, 966, 120, doi: [10.3847/1538-4357/ad3105](https://doi.org/10.3847/1538-4357/ad3105)
- Liu, T., Li, P. S., Juvela, M., et al. 2018, ApJ, 859, 151, doi: [10.3847/1538-4357/aac025](https://doi.org/10.3847/1538-4357/aac025)
- Lu, X., Zhang, Q., Liu, H. B., Wang, J., & Gu, Q. 2014, The Astrophysical Journal, 790, 84, doi: [10.1088/0004-637X/790/2/84](https://doi.org/10.1088/0004-637X/790/2/84)
- MacLaren, I., Richardson, K. M., & Wolfendale, A. W. 1988, ApJ, 333, 821, doi: [10.1086/166791](https://doi.org/10.1086/166791)

- Marsh, K. A., Whitworth, A. P., Lomax, O., et al. 2017, MNRAS, 471, 2730, doi: [10.1093/mnras/stx1723](https://doi.org/10.1093/mnras/stx1723)
- McKee, C. F., & Tan, J. C. 2002, Nature, 416, 59, doi: [10.1038/416059a](https://doi.org/10.1038/416059a)
- . 2003, ApJ, 585, 850, doi: [10.1086/346149](https://doi.org/10.1086/346149)
- Merello, M., Molinari, S., Rygl, K. L. J., et al. 2019, MNRAS, 483, 5355, doi: [10.1093/mnras/sty3453](https://doi.org/10.1093/mnras/sty3453)
- Molinari, S., Swinyard, B., Bally, J., et al. 2010, PASP, 122, 314, doi: [10.1086/651314](https://doi.org/10.1086/651314)
- Molinari, S., Schisano, E., Elia, D., et al. 2016a, A&A, 591, A149, doi: [10.1051/0004-6361/201526380](https://doi.org/10.1051/0004-6361/201526380)
- . 2016b, A&A, 591, A149, doi: [10.1051/0004-6361/201526380](https://doi.org/10.1051/0004-6361/201526380)
- Motte, F., Bontemps, S., & Louvet, F. 2018, Annual Review of Astronomy and Astrophysics, 56, 41, doi: <https://doi.org/10.1146/annurev-astro-091916-055235>
- Myers, P. C. 1983, ApJ, 270, 105, doi: [10.1086/161101](https://doi.org/10.1086/161101)

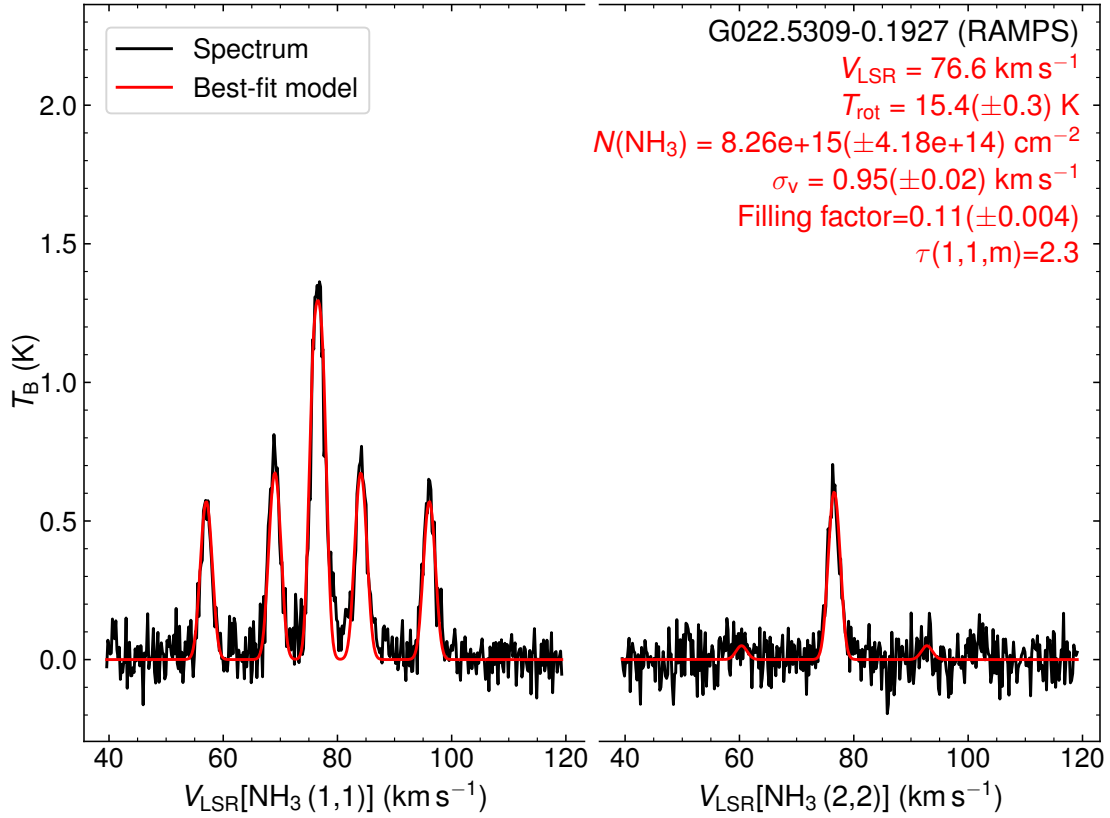


Figure 2. An example of the NH_3 line fitting using our procedure. The black lines are mean NH_3 (1,1) and NH_3 (2,2) spectra extracted from within the clump size of HMSC G022.5309-0.1927. The red lines show the best fitted model. The fitted parameters and their uncertainty are printed on the up-right corner of the plot.

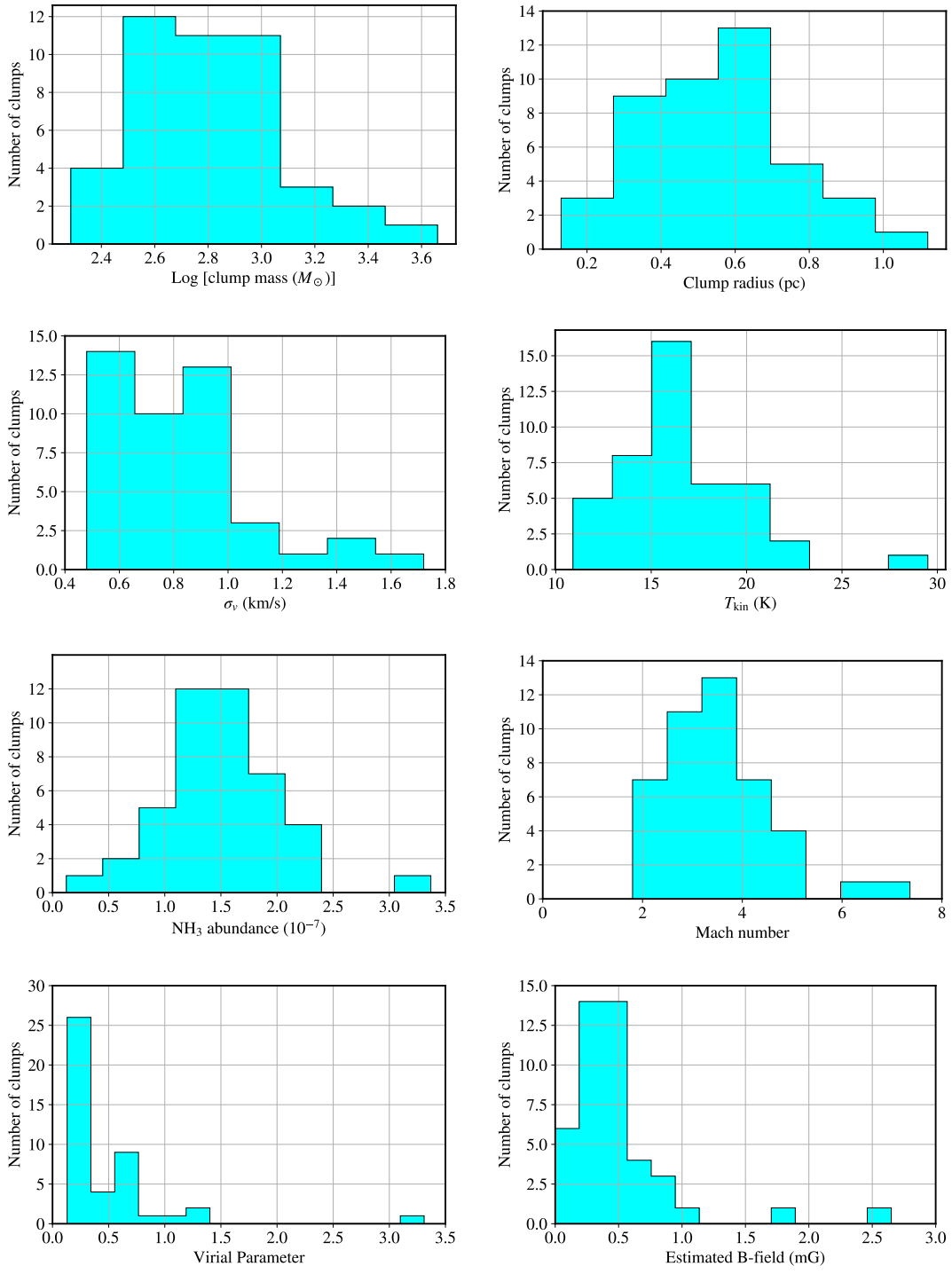
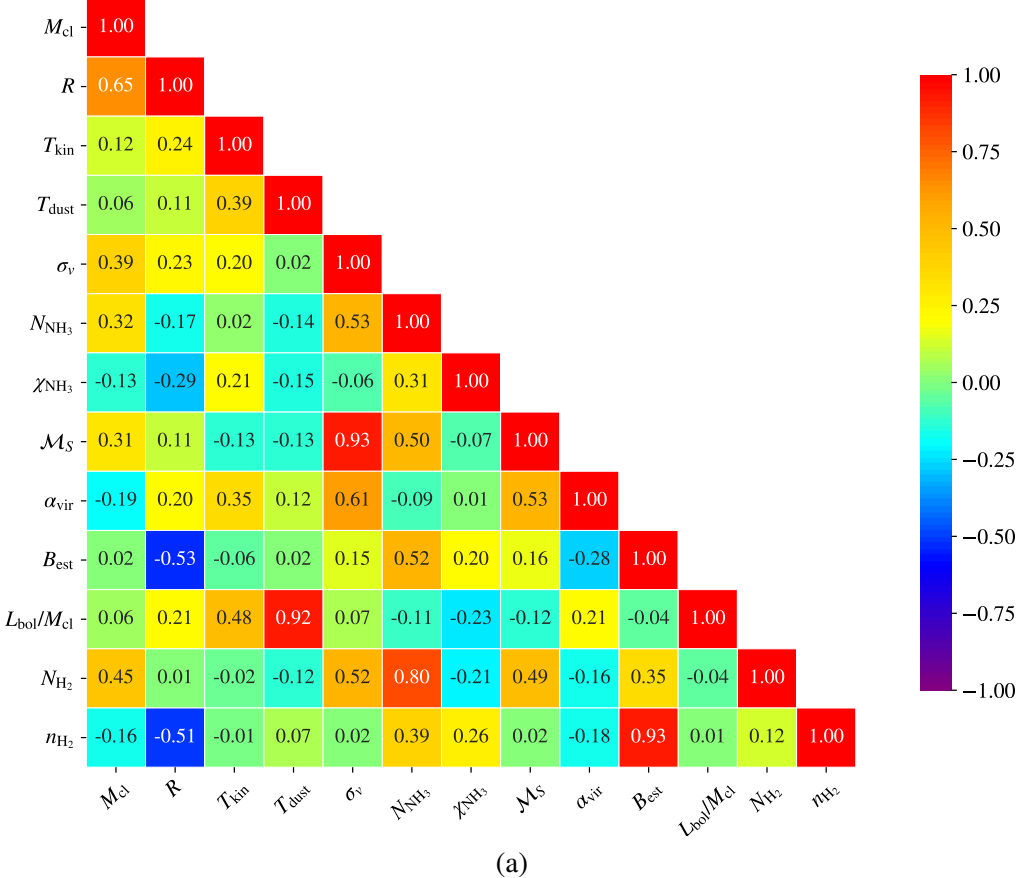
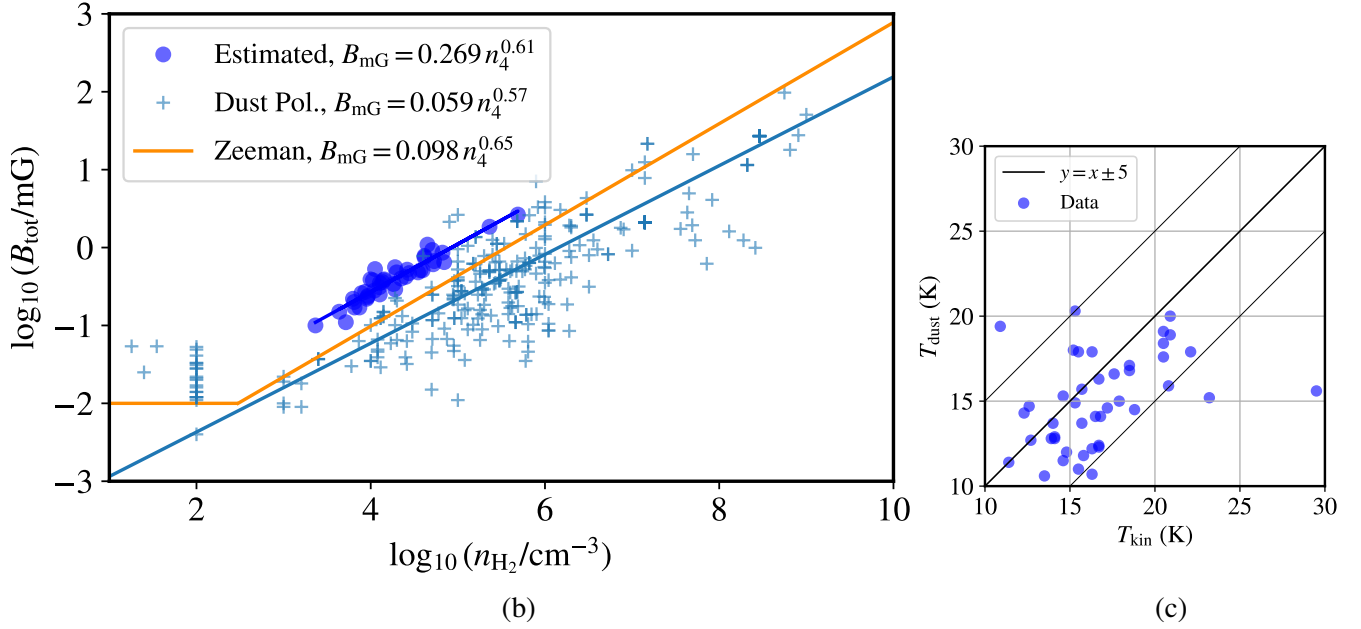


Figure 3. Histograms of basic, NH₃ fitted, and derived parameters of the HMSCs (Table 1): clump mass, equivalent radius; NH₃ fitted velocity dispersion, kinetic temperature, and NH₃ abundance; derived Mach number, virial parameter, and estimated magnetic field strength (for the 43 HMSCs with $\alpha_{\text{vir}} < 2$).



(a)



(b)

(c)

Figure 4. (a) Pearson correlation coefficient (P) matrix for the HMSCs. P is in range $[-1, 1]$, where $|P| > 0.6$ is considered to show a strong correlation. (b) Comparing the estimated B-field strength to observations. The $B_{\text{est}} - n$ relation (blue circles and line) for the HMSCs are fitted as $B_{\text{mG}} = 0.269 n_4^{0.61}$, where B_{mG} is B in units of mG and n_4 is n_{H_2} in 10^4 cm^{-3} . The 288 dust polarization measurements complied by Liu et al. (2022) are shown in crosses with a fitted line in light blue. The orange line is a fit to Zeeman splitting measurements, with a break at $n_{\text{H}_2} = 300 \text{ cm}^{-3}$, adopted from Crutcher et al. (2010). (c) The discrepancy between gas kinetic temperature and dust temperature. T_{dust} is from Yuan et al. (2017), which is derived from SED fitting to *Herschel*/HiGAL 70-500 μm continuum images at a resolution of 36.4'', comparable to the GBT NH₃ data.

- Padoan, P., Pan, L., Juvela, M., Haugbolle, T., & Ake Nordlund. 2020, *The Astrophysical Journal*, 900, 82, doi: [10.3847/1538-4357/abaa47](https://doi.org/10.3847/1538-4357/abaa47)
- Palau, A., Ballesteros-Paredes, J., Vázquez-Semadeni, E., et al. 2015, *Monthly Notices of the Royal Astronomical Society*, 453, 3785, doi: [10.1093/mnras/stv1834](https://doi.org/10.1093/mnras/stv1834)
- Pattle, K., Fissel, L., Tahani, M., Liu, T., & Ntormousi, E. 2023, in *Astronomical Society of the Pacific Conference Series*, Vol. 534, *Protostars and Planets VII*, ed. S. Inutsuka, Y. Aikawa, T. Muto, K. Tomida, & M. Tamura, 193, doi: [10.48550/arXiv.2203.11179](https://doi.org/10.48550/arXiv.2203.11179)
- Peretto, N., Fuller, G. A., Duarte-Cabral, A., et al. 2013, *A&A*, 555, A112, doi: [10.1051/0004-6361/201321318](https://doi.org/10.1051/0004-6361/201321318)
- Pillai, T., Kauffmann, J., Wyrowski, F., et al. 2011, *A&A*, 530, A118, doi: [10.1051/0004-6361/201015899](https://doi.org/10.1051/0004-6361/201015899)
- Pillai, T., Wyrowski, F., Carey, S. J., & Menten, K. M. 2006, *A&A*, 450, 569, doi: [10.1051/0004-6361:20054128](https://doi.org/10.1051/0004-6361:20054128)
- Sanhueza, P., Jackson, J. M., Zhang, Q., et al. 2017, *ApJ*, 841, 97, doi: [10.3847/1538-4357/aa6ff8](https://doi.org/10.3847/1538-4357/aa6ff8)
- Sanhueza, P., Girart, J. M., Padovani, M., et al. 2021, *ApJL*, 915, L10, doi: [10.3847/2041-8213/ac081c](https://doi.org/10.3847/2041-8213/ac081c)
- Schuller, F., Menten, K. M., Contreras, Y., et al. 2009, *A&A*, 504, 415, doi: [10.1051/0004-6361/200811568](https://doi.org/10.1051/0004-6361/200811568)
- Schuller, F., Csengeri, T., Urquhart, J. S., et al. 2017, *A&A*, 601, A124, doi: [10.1051/0004-6361/201628933](https://doi.org/10.1051/0004-6361/201628933)
- Schuller, F., Urquhart, J. S., Csengeri, T., et al. 2021, *MNRAS*, 500, 3064, doi: [10.1093/mnras/staa2369](https://doi.org/10.1093/mnras/staa2369)
- Sokolov, V., Wang, K., Pineda, J. E., et al. 2017, *A&A*, 606, A133, doi: [10.1051/0004-6361/201630350](https://doi.org/10.1051/0004-6361/201630350)
- . 2018, *A&A*, 611, L3, doi: [10.1051/0004-6361/201832746](https://doi.org/10.1051/0004-6361/201832746)
- . 2019, *ApJ*, 872, 30, doi: [10.3847/1538-4357/aafaff](https://doi.org/10.3847/1538-4357/aafaff)
- Stephens, I. W., Myers, P. C., Zucker, C., et al. 2022, *ApJL*, 926, L6, doi: [10.3847/2041-8213/ac4d8f](https://doi.org/10.3847/2041-8213/ac4d8f)
- Sun, S., Wang, K., Liu, X., & Xu, F. 2024, *ApJL*, in press, arXiv:2409.01895, doi: [10.3847/2041-8213/ad77ce](https://doi.org/10.3847/2041-8213/ad77ce)
- Svoboda, B. E., Shirley, Y. L., Battersby, C., et al. 2016, *ApJ*, 822, 59, doi: [10.3847/0004-637X/822/2/59](https://doi.org/10.3847/0004-637X/822/2/59)
- Tackenberg, J., Beuther, H., Henning, T., et al. 2012, *A&A*, 540, A113, doi: [10.1051/0004-6361/201117412](https://doi.org/10.1051/0004-6361/201117412)
- Tafalla, M., Myers, P. C., Caselli, P., & Walmsley, C. M. 2004, *A&A*, 416, 191, doi: [10.1051/0004-6361:20031704](https://doi.org/10.1051/0004-6361:20031704)
- Traficante, A., Fuller, G. A., Peretto, N., Pineda, J. E., & Molinari, S. 2015, *Monthly Notices of the Royal Astronomical Society*, 451, 3089, doi: [10.1093/mnras/stv1158](https://doi.org/10.1093/mnras/stv1158)
- Traficante, A., Duarte-Cabral, A., Elia, D., et al. 2018, *Monthly Notices of the Royal Astronomical Society*, 477, 2220, doi: [10.1093/mnras/sty798](https://doi.org/10.1093/mnras/sty798)
- Vázquez-Semadeni, E., Ballesteros-Paredes, J., & Rodríguez, L. F. 1997, *ApJ*, 474, 292, doi: [10.1086/303432](https://doi.org/10.1086/303432)
- Walmsley, C. M., & Ungerechts, H. 1983, *A&A*, 122, 164
- Wang, C., & Wang, K. 2023, *A&A*, 674, A46, doi: [10.1051/0004-6361/202244525](https://doi.org/10.1051/0004-6361/202244525)
- Wang, C., Wang, K., Xu, F.-W., et al. 2024, *A&A*, 681, A51, doi: [10.1051/0004-6361/202347024](https://doi.org/10.1051/0004-6361/202347024)
- Wang, K. 2018, *Research Notes of the American Astronomical Society*, 2, 52, doi: [10.3847/2515-5172/aacb29](https://doi.org/10.3847/2515-5172/aacb29)
- Wang, K., Wu, Y. F., Ran, L., Yu, W. T., & Miller, M. 2009, *A&A*, 507, 369, doi: [10.1051/0004-6361/200811104](https://doi.org/10.1051/0004-6361/200811104)
- Wang, K., Zhang, Q., Wu, Y., Li, H.-b., & Zhang, H. 2012, *ApJL*, 745, L30, doi: [10.1088/2041-8205/745/2/L30](https://doi.org/10.1088/2041-8205/745/2/L30)
- Wang, K., Zhang, Q., Testi, L., et al. 2014, *MNRAS*, 439, 3275, doi: [10.1093/mnras/stu127](https://doi.org/10.1093/mnras/stu127)
- Wang, Y., Zhang, Q., Pillai, T., Wyrowski, F., & Wu, Y. 2008, *ApJL*, 672, L33, doi: [10.1086/524949](https://doi.org/10.1086/524949)
- Wienen, M., Wyrowski, F., Menten, K. M., et al. 2018, *A&A*, 609, A125, doi: [10.1051/0004-6361/201526384](https://doi.org/10.1051/0004-6361/201526384)
- Wienen, M., Wyrowski, F., Schuller, F., et al. 2012, *A&A*, 544, A146, doi: [10.1051/0004-6361/201118107](https://doi.org/10.1051/0004-6361/201118107)
- Xu, F., Wang, K., He, Y., et al. 2023a, *ApJS*, 269, 38, doi: [10.3847/1538-4365/acfee2](https://doi.org/10.3847/1538-4365/acfee2)
- Xu, F.-W., Wang, K., Liu, T., et al. 2023b, *MNRAS*, 520, 3259, doi: [10.1093/mnras/stad012](https://doi.org/10.1093/mnras/stad012)
- Yu, S., Jiang, Z., Yang, Y., Chen, Z., & Feng, H. 2022, *Research in Astronomy and Astrophysics*, 22, 095014, doi: [10.1088/1674-4527/ac7d9d](https://doi.org/10.1088/1674-4527/ac7d9d)
- Yuan, J., Wu, Y., Ellingsen, S. P., et al. 2017, *ApJS*, 231, 11, doi: [10.3847/1538-4365/aa7204](https://doi.org/10.3847/1538-4365/aa7204)
- Yuan, J., Li, J.-Z., Wu, Y., et al. 2018, *ApJ*, 852, 12, doi: [10.3847/1538-4357/aa9d40](https://doi.org/10.3847/1538-4357/aa9d40)

- Yue, N.-N., Li, D., Zhang, Q.-Z., et al. 2021, Research in Astronomy and Astrophysics, 21, 024, doi: [10.1088/1674-4527/21/1/24](https://doi.org/10.1088/1674-4527/21/1/24)
- Zhang, Q., & Wang, K. 2011, ApJ, 733, 26, doi: [10.1088/0004-637X/733/1/26](https://doi.org/10.1088/0004-637X/733/1/26)
- Zhang, Q., Wang, K., Lu, X., & Jiménez-Serra, I. 2015, ApJ, 804, 141, doi: [10.1088/0004-637X/804/2/141](https://doi.org/10.1088/0004-637X/804/2/141)
- Zhang, Q., Qiu, K., Girart, J. M., et al. 2014, ApJ, 792, 116, doi: [10.1088/0004-637X/792/2/116](https://doi.org/10.1088/0004-637X/792/2/116)
- Zhang, S., Wang, K., Liu, T., et al. 2023, MNRAS, 520, 322, doi: [10.1093/mnras/stad011](https://doi.org/10.1093/mnras/stad011)
- Zhou, J.-W., Liu, T., Evans, N. J., et al. 2022, MNRAS, 514, 6038, doi: [10.1093/mnras/stac1735](https://doi.org/10.1093/mnras/stac1735)